MATERIALS CHEMISTRY FRONTIERS

CHINESE CHEMICAL SOCIETY

ROYAL SOCIETY OF CHEMISTRY

RESEARCH ARTICLE

View Article Online
View Journal | View Issue

Cite this: *Mater. Chem. Front.*, 2023, 7, 545

Theoretical insights into the rational design of small organic phototheranostic agents for promoting image-guided cancer surgery†

Jia Zhang,[a] Junfang Yang,[b] Yi Zeng,[a] Ze-Sheng Li [a] and Xiaoyan Zheng *[ac]

Received 25th November 2022,
Accepted 6th January 2023

DOI: 10.1039/d2qm01227h

rsc.li/frontiers-materials

To realize the precise regulation of phototheranostics for AIE luminogens (AIEgens), unraveling the molecular configuration, molecular packing and phototheranostic property relationships is of vital importance. Through a multiscale modeling protocol that combines molecular dynamics simulations, implicit polarizable continuum models and thermal vibration correlation function formalism coupled quantum mechanics/molecular mechanics models, the inherent mechanism of two structurally similar donor–(π)–acceptor-type AIEgens (TI and TSSI) with significantly different performances in phototheranostics were firstly explored. It is found that TSSI with additional thiophene rings as a bridge largely improves the phototheranostic properties, which includes a redshifted emission, a high photothermal conversion efficiency (PCE) and a good intersystem crossing (ISC) efficiency. Based on that, we propose a molecular design strategy and design a series of AIEgens *via* structural modification of the acceptor moiety or extending the π-bridge of TSSI. It is found that, TSSSSI is predicted to be a potential candidate for NIR-II fluorescence imaging guided photodynamic and photothermal therapy applications owing to its excellent fluorescence efficiency, efficient ISC process, and emission spectrum in the NIR-II region. Lastly, the fluorescence quantum efficiency enhancement of TSSI upon aggregation was caused by suppressing the rotational vibrations in the low-frequency region. Our theoretical protocol is general and applicable to other AIEgens, thus laying a solid foundation for the rational design of advanced AIEgens for applications in phototheranostics.

Introduction

Phototheranostic strategies using organic luminescence are experiencing a rapid development, because of their high accuracy, high efficiency and non-invasive nature,[1–5] which overcome the disadvantages of conventional tumor treatment methods with a high surgical risk and limited efficacy.[6,7] In current diagnostic technology, fluorescence imaging (FLI) has a high sensitivity, a fast response and is non-invasive, although it is limited in its penetration depth.[8,9] By contrast, photoacoustic imaging (PAI) has a centimeter-scale imaging depth, but lacks sensitivity.[10,11] Photothermal imaging (PTI) shows good temperature sensitivity and a real-time monitoring ability.[12,13] Photothermal therapy (PTT) and photodynamic therapy (PDT) are both light-controllable and non-invasive, but have heat shock effects and hypoxic nature, respectively.[14,15] The combination of different diagnostic and therapeutic techniques can overcome these intrinsic shortcomings and achieve both accurate diagnosis and a good treatment efficiency.[16] In addition, the absorption and emission of long wavelengths in near-infrared (NIR) region are important in photo-theranostic applications *in vivo*, because they help to achieve better penetration into tissue with less damage[17] and a high signal-to-noise ratio.[18,19]

The performance of phototheranostics is closely related to the relative contributions of the different decay channels of photoexcited molecules. According to the Jablonski diagram, there are three key dissipative channels of excited state energies. First is the radiative channel, which generates fluorescence and affords FLI.[20,21] The second is the internal conversion process through thermal vibrations, which is utilized in PTI, PAI and PTT.[14] The third is the intersystem

[a] *Key Laboratory of Cluster Science of Ministry of Education, Key Laboratory of Medicinal Molecule Science and Pharmaceutics Engineering of Ministry of Industry and Information Technology, Beijing Key Laboratory of Photoelectronic/Electrophotonic Conversion Materials, School of Chemistry and Chemical Engineering, Beijing Institute of Technology, 100081, Beijing, P. R. China. E-mail: xiaoyanzheng@bit.edu.cn*

[b] *School of Chemical Sciences, University of Chinese Academy of Sciences, Beijing, 100049, P. R. China*

[c] *Guangdong Provincial Key Laboratory of Luminescence from Molecular Aggregates (South China University of Technology), Guangzhou, 510640, China*

† Electronic supplementary information (ESI) available. See DOI: https://doi.org/10.1039/d2qm01227h

crossing (ISC) process, which produces reactive oxygen species (ROS) for PDT.[22–24] The three decay channels of excited states compete with each other, and the energy partition between these different decay channels influences the probabilities of the different functions for phototheranostics. AIE luminogens (AIEgens) are ideal candidates for phototheranostics. AIEgens with non-planar twisted conformations pack loosely in the condensed phase, which is not only beneficial for fluorescent emission but also keeps the intramolecular motions active in the aggregates, and this could well balance the energy partition of the different decay channels of the excited states.[3,12,13,19,25–30] The precise control of the energy partition on the different decay channels of AIEgens is key to regulating their performance in phototheranostics.

Nonetheless, the development of AIEgen-based organic luminescence for phototheranostics requires the optimization of many factors, such as the absorption/emission wavelength, the photothermal conversion efficiency, spin–orbit coupling (SOC), chemical stability and so on. These factors interplay with each other and cannot be optimized separately; therefore, it is a great challenge for researchers to design organic AIEgens through trial-and-error. Unraveling the microscopic mechanisms behind the phototheranostics of organic luminescence is a key prerequisite for the precise design of organic luminescence with good performance for phototheranostics; these remain elusive, however, due to the limited spatial-temporal resolution of current experimental techniques. Multiscale modeling has played an important role in elucidating the relationship between the molecular configuration, molecular packing and phototheranostic properties of AIEgens and understanding their system-dependent performance in phototheranostics, which is beneficial for the rational design of AIEgens at minimal cost compared with the trial-and-error screening approach of experiments.[31–35] This can be exemplified by two representative AIEgens: TI and TSSI. As shown in Scheme 1, TI consists of triphenylamine as the donor (D) and the 1,3-bis(dicyanomethylidene) indane moiety as the acceptor (A); for TSSI, except for the same D and A, it also comprises two additional thiophene rings as a π-bridge. Therefore, TI and TSSI are D–A and D–π–A type molecules, respectively, and their only difference is that TSSI contains the additional thiophene rings as the π-bridge. Although TI and TSSI have similar chemical structures, they display distinct performances in phototheranostics. Experimentally, TI and TSSI are both AIEgens, where TSSI displays much redder absorption (NIR-I) and emission (NIR-II) spectra than TI. In addition, TSSI simultaneously demonstrates a higher PCE and a superior ROS production efficiency than TI.[36] In contrast to TI, TSSI shows an unprecedented performance in NIR-II FLI-PAI–PTI trimodal-imaging-guided PDT–PTT synergistic therapy.[36]

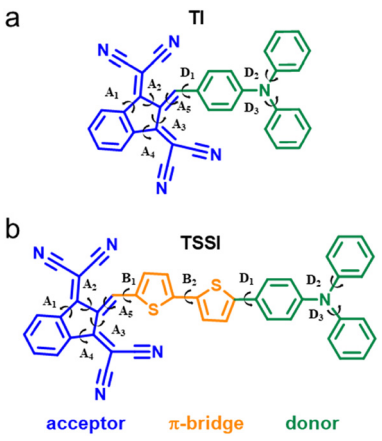

Scheme 1 Chemical structures of (a) TI and (b) TSSI. The acceptor, π-bridge, and donor are labeled in blue, orange and green, respectively, and the corresponding dihedral angles are $A_{n=1-5}$, $B_{n=1,2}$, and $D_{n=1-3}$, respectively.

In this contribution, we adopt a theoretical protocol that combines molecular dynamics simulations (MD), implicit polarizable continuum models (PCM) and hybrid quantum mechanics/molecular mechanics (QM/MM) models (see Fig. S1, ESI†)[37,38] to systematically explore the striking difference in the phototheranostic performance of TI and TSSI, which have similar chemical structures, at the microscopic level. Based on these theoretical calculations, we further design a series of AIEgens and study their potential abilities in phototheranostics to systematically optimize the performance of the AIEgens with respect to the target function of phototheranostics, such as NIR-II FLI. Finally, the AIE mechanism of the representative AIEgen TSSI is demonstrated.

Results and discussion

Phototheranostic properties of TI and TSSI

The structural changes in both TI and TSSI upon excitation were demonstrated. For clarity, the key dihedral angles of the acceptor, the π-bridge and the donor are defined as A_n (A_1, A_2, A_3, A_4, and A_5), B_n (B_1 and B_2) and D_n (D_1, D_2, and D_3), respectively (see Scheme 1). Moreover, the changes of the TI and TSSI bond lengths (within 0.03 Å) and bond angles (within 1.1°) are negligible (see more details in Table S2, ESI†). This indicates that TSSI is more flexible and displays more obvious structural modifications than TI in dilute solution. For example, the change in A_2 for TSSI (28.3°) is much larger than that for TI (3.3°) (see Fig. 1a and Table S2, ESI†). Upon excitation, the A backbone of TI becomes more planar and that of D is more twisted, as reflected by the decreased dihedral angles of the A moiety (A_1, A_2, A_3, A_4 and A_5) and the increased dihedral angles of the D moiety (D_1, D_2 and D_3). By comparison, the configuration of TSSI becomes more planar after excitation, because all the extracted dihedral angles of D, π-bridge and A are decreased, indicating that the introduction of the π-bridge effectively improves the conjugation of TSSI (Fig. 1b, c and Table S2, ESI†). The statistical population of the key dihedral angles of TSSI obtained from MD simulations also shows wider distributions than that of TI (Fig. 1d). For example, the distribution of D_1 in TSSI is in range of −180° to 180°, while that of TI is only in range of 10° to 180°; at the same time, B_1 and B_2 of the additional thiophene rings in TSSI also have a certain range of distributions (Fig. 1d). This indicates that the dynamic

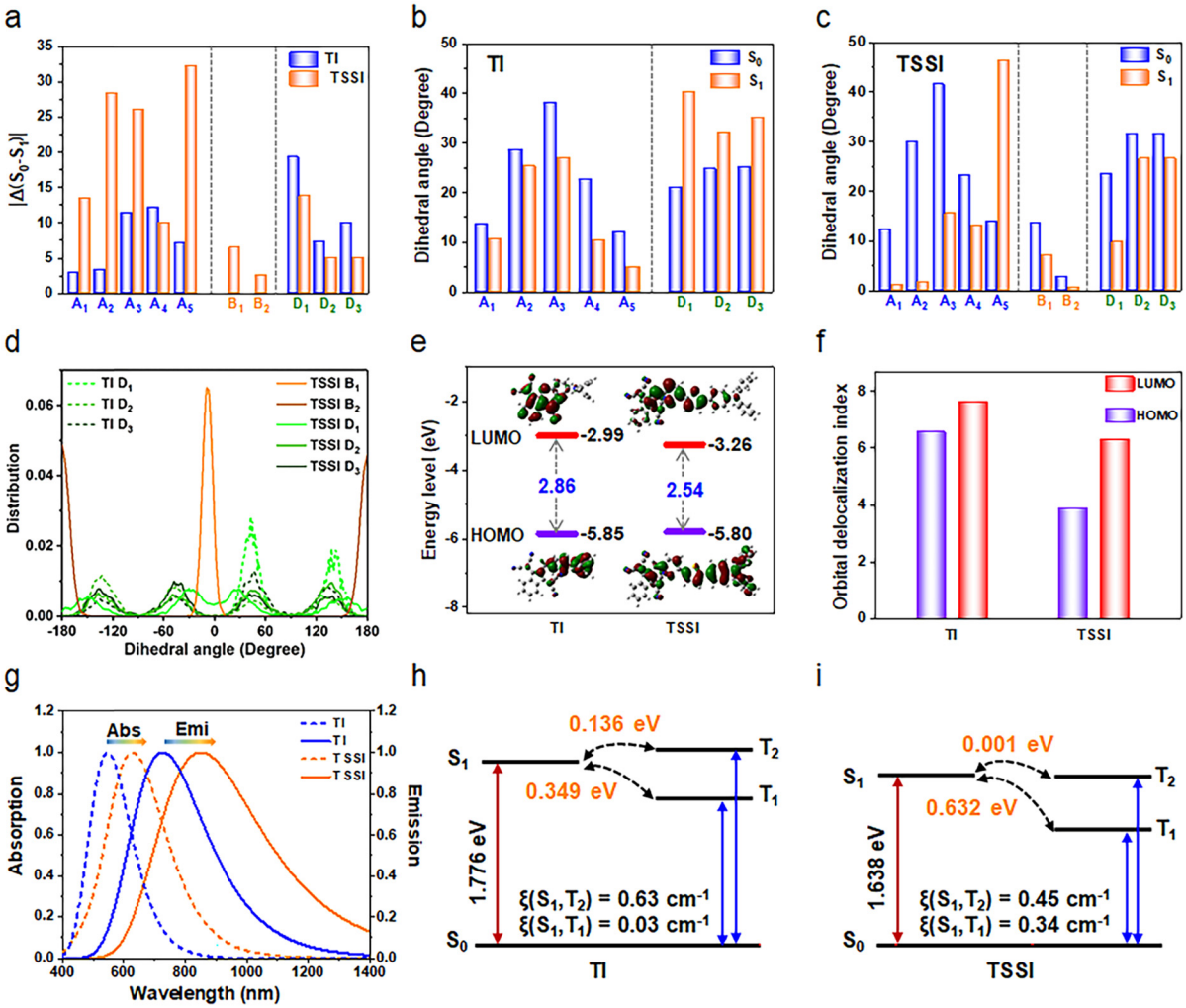

Fig. 1 (a) Modification of dihedral angles between S_0 and S_1 of optimized TI and TSSI in dilute solution. (b and c) Selected dihedral angles of TI and TSSI at both S_0 and S_1. (d) Distributions of the representative dihedral angles of TI and TSSI based on MD trajectories. (e) HOMO, LUMO and energy gaps (ΔE_g), as well as (f) the orbital delocalization index of the HOMO and LUMO for the S_1-geometry of TI and TSSI in dilute solution. (g) Calculated absorption and emission spectra, as well as (h and i) the ΔE_{ST} and spin–orbit couplings (ξ) of TI and TSSI in solution.

conformational changes of TSSI in aqueous solution are much easier than in TI (see the representative conformations of TI and TSSI in Fig. S2, ESI†). Therefore, TSSI is more flexible than TI, and it may release more heat energy vibrationally through the non-radiative decay channel of the excited state, which is beneficial for improving the performance in PTI, PAI and PTT.

The S_1 transition orbitals of TI and TSSI are both mainly contributed by HOMO → LUMO, although HOMO−1 → LUMO plays a minor role (Fig. 1e, Fig S3 and Table S3, ESI†). As shown in Fig. 1e, TI has a twisted intramolecular charge transfer (TICT) feature with the HOMO and LUMO distributed on the D and A moieties, respectively. TSSI shows a hybrid local excited (LE) and charge transfer (CT) state, with the HOMO and LUMO delocalized over almost the entire TSSI skeleton, because the introduced π-bridge largely improves the backbone planarity and enlarges the effective conjugation length for the S_1 of TSSI. Accordingly, the ΔE_g of TSSI (2.54 eV) is smaller than that of TI (2.86 eV) (see Fig. 1e). The orbital delocalization can be quantitatively characterized *via* the orbital delocalization index (ODI), where the smaller the ODI, the larger the extent of orbital delocalization. Clearly, the ODI of both the HOMO and LUMO of TSSI are smaller than those of TI, which is supportive of the increased planarity and conjugation of TSSI induced by the π-bridge (Fig. 1f). The absorption and emission spectra of TSSI are both redshifted compared with TI, because of the better planarity and the smaller ΔE_g of TSSI (Fig. 1g), in good agreement with the experimental results.[36] In particular, the absorption and emission spectra of TSSI fall in the NIR-I and NIR-II regions with peak maxima at 628 nm and 850 nm, respectively, which is also beneficial for its FLI application *in vivo*.[36]

The ISC process is estimated from the energy gap (ΔE_{ST}) between S_1 and the low-lying triplet states (T_1 or T_2), as well as the SOC (ξ) values. Generally, reducing ΔE_{ST} or increasing ξ can effectively increase the ISC efficiency and enhance the PDT performance. As shown in Fig. 1h and i, the negligible ΔE_{ST}

(0.001 eV) and the excellent ξ (0.45 cm^{-1}) between S_1 and T_2 for TSSI can realize a more efficient ISC process than TI, which shows ΔE_{ST} (0.136 eV) and ξ (0.63 cm^{-1}). Therefore, TSSI has a better performance in PDT applications than TI, consistent with experimental results.[36]

Above all, in contrast to TI, the introduction of the thiophene-ring bridge between the donor and acceptor of TSSI largely improves its performance of the phototheranostic properties, which not only redshifts the absorption and emission spectra but also improves the PCE due to the boosting of non-radiative decay pathways. In addition, the small ΔE_{ST} and the large ξ value also enhance the PDT function. Therefore, TSSI has a better phototheranostic performance than TI, in good agreement with experimental results.[36]

Molecular design

Further molecular design based on TSSI was performed to deepen our understanding of the structure–property relationship of the AIEgens on the phototheranostic performance. Two molecular design strategies were proposed to optimize the specific functions of the phototheranostics. (i) We introduced an additional electron-deficient cyano group at 4-position or 5-position of the indane moiety of TSSI, which are designated as *o*-TSSI or *m*-TSSI, respectively (see Fig. 2). Introducing a cyano group into the A moiety of TSSI only not can increase the electron-withdrawing ability of the A moiety and enhance the separation of D and A but also incorporates the steric hindrance of the cyano group into the molecular conformations and phototheranostic properties. (ii) We extended the π-bridge of TSSI to three or four thiophene rings, designated as TSSSI or TSSSSI, respectively, to further improve the conjugation length and red-shift the absorption and emission spectra of TSSI (see Fig. 2).

As shown in Fig. 3a and Scheme S2 (ESI†), the key dihedral angles of the A moiety (particularly for A_1 and A_2) of *o*-TSSI for both S_0 and S_1 are much larger than those of the other four AIEgens, TSSI, *m*-TSSI, TSSSI and TSSSSI, because of the steric hindrance of the 4-position of the indane moiety of *o*-TSSI. For example, A_1 increases from 12.2° and 1.2° for TSSI to 30.5° and 28.4° for *o*-TSSI for S_0 and S_1, respectively (Tables S2 and S4, ESI†). Therefore, the introduction of the additional cyano group at the 4-position of *o*-TSSI increases the steric effect of the A moiety and results in a more distorted conformation for *o*-TSSI (Fig. S4, ESI†). By contrast, for *m*-TSSI, the dihedral angles of the D, π-bridge and A moieties are all similar to those of TSSI, indicating the neglectable steric hindrance from introducing the cyano group at the 5-position of the indane moiety (Fig. S4 and Tables S2, S4, ESI†). Lengthening the π-bridge to three and four thiophene rings can enhance the planarity of the π-bridge (supportive of the small B_3 and B_4 in Fig. 3a, Fig. S4 and Table S4, ESI†) and enlarge the conjugation length of TSSSI and TSSSSI; therefore, the absorption and emission spectra of TSSSI and TSSSSI are more redshifted than TSSI.

Similar to TSSI, all four designed AIEgens display hybrid LE and CT features, and the transition orbitals for S_1 are dominated by the HOMO → LUMO transition, with the HOMO mainly distributed on the D and π-bridge, and the LUMO distributed on the A and π-bridge, respectively (see Fig. S5 and Table S5, ESI†). For *o*-TSSI and *m*-TSSI, the introduced cyano group effectively increases the electron-withdrawing ability of the A moiety and enhances the degree of separation between the hole and the electron (see Fig. S6, ESI†); therefore, the ΔE_g values of *o*-TSSI and *m*-TSSI (2.52 eV and 2.47 eV) are smaller than that of TSSI (2.54 eV). In addition, the ΔE_g values of TSSSI and TSSSSI are decreased to 2.34 eV and 2.23 eV because of the increased conjugation length and planarity after lengthening the π-bridge of TSSI (Fig. 3a and b). Therefore, relative to TSSI, all the absorption and emission spectra of *m*-TSSI, TSSSI, and TSSSSI are redshifted with maximum emission wavelengths of 861 nm, 893 nm and 918 nm, respectively (Fig. 3c). It is clear that the absorption and emission spectra of TSSSSI cover almost the whole NIR-I and NIR-II regions. It is noted that the fluorescent emission of *o*-TSSI is blueshifted because of the torsional conformations induced by the steric hindrance of the additional cyano group at the 4-position of the indane moiety. Therefore, the strategy of lengthening the π-bridge is more conducive to the spectral redshift and is

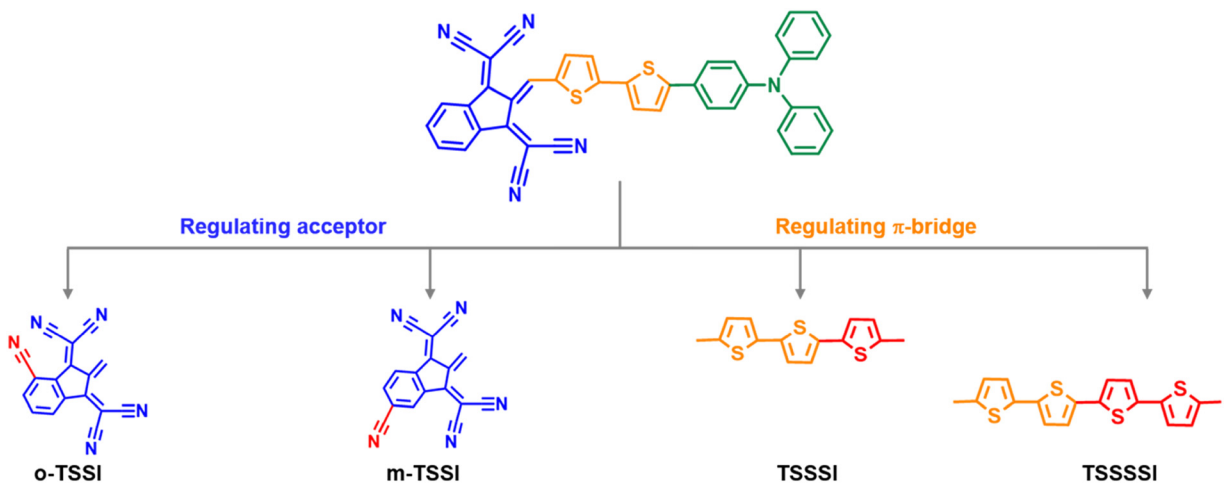

Fig. 2 Schematic illustration of the design strategies of the four organic molecules based on TSSI: *o*-TSSI, *m*-TSSI, TSSSI, and TSSSSI.

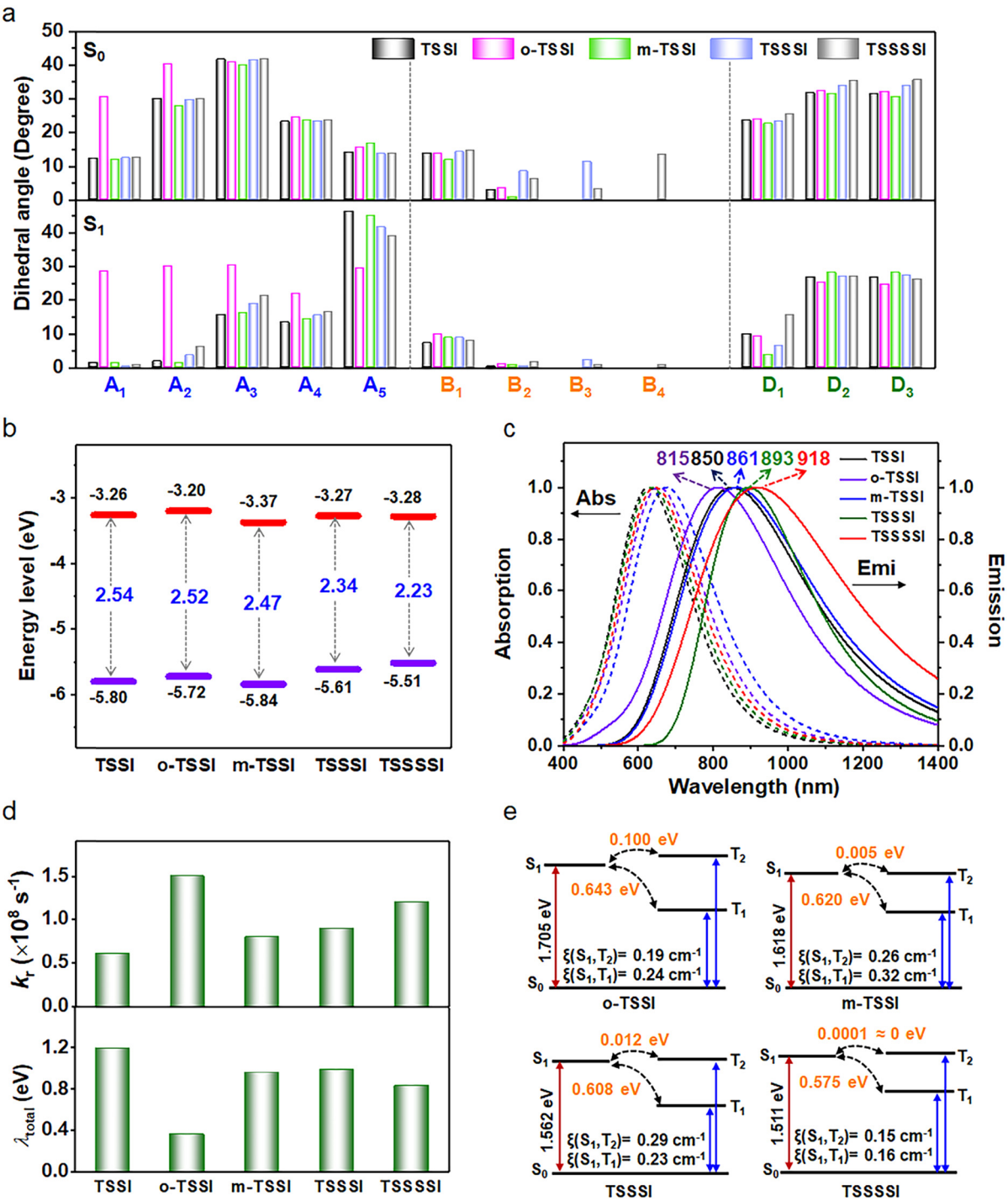

Fig. 3 Structural and photophysical parameters of TSSI and four designed AIEgens: *o*-TSSI, *m*-TSSI, TSSSI and TSSSSI. (a) Selected dihedral angles for S_0 and S_1. (b) HOMO, LUMO and ΔE_g of the S_1 geometry. (c) Absorption and emission spectra. (d) Radiative rate constant (k_r) and total reorganization energy (λ_{total}) values. (e) Calculated ΔE_{ST} and spin–orbit coupling (ξ) values.

more effective for improving the FLI performance for phototheranostics *in vivo*.

The fluorescence quantum efficiency (Φ_F) is determined *via* the radiative decay rate (k_r) and the internal conversion rate constant (k_{ic}). The k_r value is calculated using the simple spontaneous emission relationship, whereas k_{ic} can be characterized *via* the reorganization energy (λ), and these are useful parameters for measuring the extent of electron–vibration coupling. In general, the increase in λ implies a larger k_{ic}. As shown in Fig. 3d and Table S5 (ESI†), the k_r values of the four designed compounds all increase from 0.6×10^8 s^{-1} (TSSI) to 1.5×10^8 s^{-1} (*o*-TSSI), 0.8×10^8 s^{-1} (*m*-TSSI), 0.9×10^8 s^{-1}

(TSSSI), and 1.2×10^8 s^{-1} (TSSSSI), respectively; simultaneously, λ_{total} is reduced from 1.2 eV (TSSI) to 0.4 eV (*o*-TSSI), 1.0 eV (*m*-TSSI), 1.0 eV (TSSSI), and 0.8 eV (TSSSSI). In particular, *o*-TSSI with the cyano group at the 4-position of the indane moiety has the largest k_r and the smallest λ_{total}; therefore, this additional cyano group can effectively restrict the intramolecular vibrations of *o*-TSSI and improve its fluorescent emission. In addition, TSSSSI, with longest π-bridge, displays a larger k_r and a smaller λ_{total} than those of TSSI, and shows better FLI than TSSI. Therefore, both *o*-TSSI *via* the introduction of the additional cyano group at the indane 4-position and TSSSSI with the lengthened bridge dimension are beneficial for FLI.

Then, ΔE_{ST} and ξ were calculated to qualitatively estimate the ISC process (Fig. 3e). It is found that, ΔE_{T2-S1} is reduced successively from *o*-TSSI (0.100 eV) to TSSSI (0.012 eV), *m*-TSSI (0.005 eV), TSSI (0.001 eV) and TSSSSI (~0 eV), and the ΔE_{T2-S1} value of TSSSSI is the smallest at almost equal to zero. Simultaneously, the corresponding ξ_{T2-S1} values of all the compounds are of the same order of magnitude (0.19 cm^{-1}, 0.29 cm^{-1}, 0.26 cm^{-1} 0.45 cm^{-1} and 0.15 cm^{-1}), indicating the relative facilitated ISC process and the good performance for PDT (Fig. 3e). Therefore, the TSSSSI with the π-bridge lengthened to four thiophene rings is predicted to be a potential candidate for phototheranostic applications owing to its excellent FLI, efficient ISC process, and emission spectrum in the NIR-II region.

Aggregation effect

The hybrid QM/MM models of representative amorphous aggregates were set up to elucidate the aggregation effects of TSSI and to systematically investigate the influence of the molecular packing on the photophysical properties of TSSI. Considering the irregular molecular packing of TSSI in amorphous aggregates, three representative conformations were randomly selected and the QM/MM models set up accordingly to calculate their photophysical properties (Fig. 4a). It was found that the TSSI monomer is more flexible compared with as amorphous aggregates, due to the dense molecular packing, and the structural modifications upon excitation are sharply decreased after aggregation (Fig. 4b and Tables S2, S6, ESI†). For example, the structural modification of A_2 and A_5 of TSSI are largely reduced from 28.3° and 32.2° in the dispersed state to 4.4° and 4.9° in an amorphous aggregate, respectively. Moreover, the backbone of TSSI suffers a significant distortion from linear to bent upon aggregation, which is supported by the variation of B_1 and B_2 from 7.1° and 0.2° in the dispersed state to 18.8° and 37.8° in an amorphous aggregate for the S_1-geometry (Fig. S7, ESI†).

The major transition orbitals, HOMO and LUMO, of TSSI are localized at the D and A moieties, respectively (Fig. 4c, Fig. S8, and Table S7, ESI†), showing the ICT features. Due to the twisted backbone and the reduced conjugation after aggregation, the corresponding ΔE_g of TSSI in the aggregate (2.62 eV) is larger than that of the dispersed form (2.54 eV), and therefore the emission spectrum of TSSI is blueshifted upon aggregation (Fig. 4c, d and Fig. S9–S11, ESI†). Moreover, the absorption and emission spectra of TSSI in the amorphous aggregate fall in NIR-I and NIR-II regions with peaks at 706 nm and 824 nm, respectively. Relative to TSSI in the dispersed state, the emission spectrum of the amorphous aggregate is blueshifted.

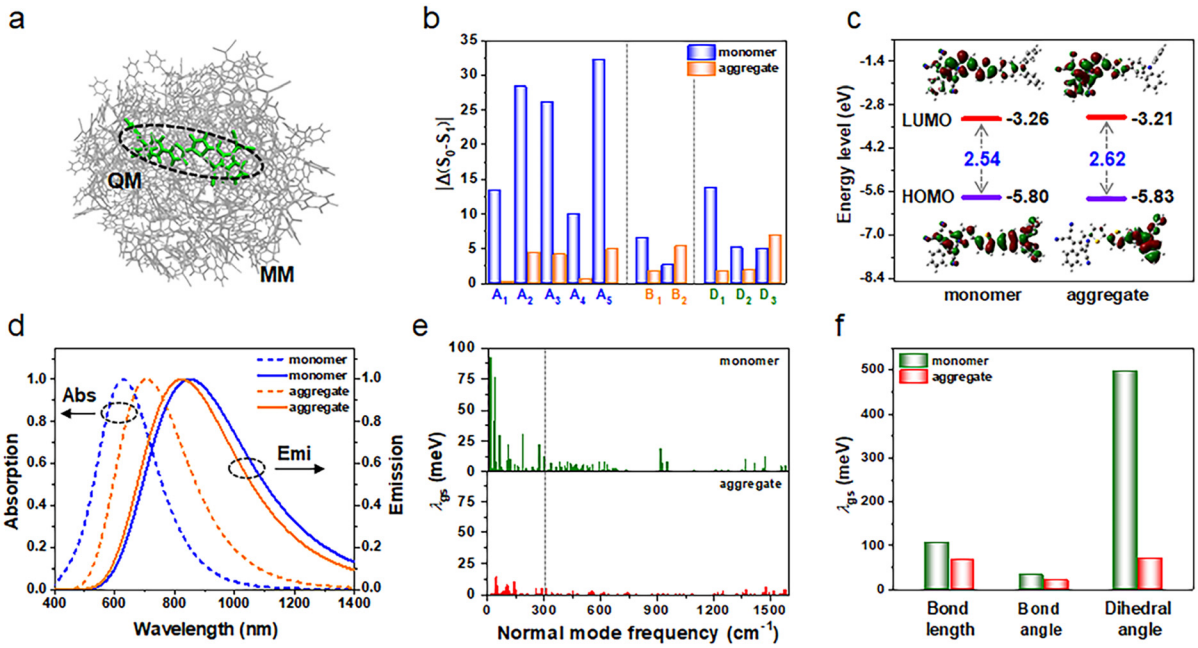

Fig. 4 (a) QM/MM model of TSSI as an amorphous aggregate, where one central TSSI was selected as the QM region and the others were set as the MM region. (b) Structural modification between S_0 and S_1, as well as (c) the HOMO, LUMO and energy gap (ΔE_g) for the S_1-geometry of TSSI in monomer and amorphous aggregate forms. (d) Calculated absorption and emission spectra of TSSI in monomer and amorphous aggregate forms. (e and f) Projection of the reorganization energy in the ground state (λ_{gs}) on the normal mode frequency and internal coordinates of TSSI in monomer and amorphous aggregate forms.

The k_r, k_{ic} and Φ_F data of TSSI in the amorphous aggregate were also estimated using the thermal vibration correlation function protocol through the MOMAP program.[39–41] The calculated k_r and k_{ic} values of TSSI in the amorphous aggregate are 2.9×10^7 s^{-1} and 6.6×10^6 s^{-1}, respectively, and the corresponding Φ_F is 81.5% (Table S7, ESI†). As reported in previous studies,[32,42–45] k_r is immune to the environment, and the k_r of TSSI in solution and the amorphous aggregate are of the same order of magnitude. By contrast, k_{ic} is quite sensitive to the environment and is closely related to λ. It was found that the λ_{total} of TSSI in dilute solution is 1.2 eV, whereas it decreases to 0.4 eV in the aggregated state (Table S7, ESI†), implying the much larger k_{ic} of TSSI in solution compared with that as an amorphous aggregate; therefore, the Φ_F of TSSI in the aggregate is improved upon aggregation. To gain more theoretical insights into the suppressed non-radiative channel in the aggregated state, we further projected the λ_{gs} values of TSSI in both solution and the aggregated state for S_0 into the vibrational normal modes (Fig. 4e). It can be seen that the λ_{gs} values of TSSI are much smaller as aggregates than in dilute solution, particularly for the low-frequency region (<300 cm^{-1}) (see Fig. 4e). Moreover, the summation of λ_{gs} for TSSI in the low-frequency region in solution and in the aggregated form is 411 meV and 97 meV, respectively. These findings indicate that the energy dissipation pathways are easily blocked *via* low-frequency components upon aggregation. To clarify the relationship between the energy dissipative channel and the molecular structure, we projected the λ_{gs} of TSSI in both the solution and aggregated form onto the internal coordinates (Fig. 4f). It is noted that the contribution from the dihedral angles decreases from 496 meV in solution to 70 meV in the aggregated state, while the changes for the bond length and bond angle are negligible (Fig. 4f). The major components of the dihedral angles are associated with the out-of-plane motions of the A moieties, consistent with analysis of the structural modifications in Fig. 4b. These results confirm the crucial role of the phenyl-ring motions of the A-moiety in determining the photophysical properties of TSSI, which is fully consistent with the structural modification from S_0 to S_1 (Fig. 4b).

Conclusions

In summary, the underlying mechanisms of the dramatically different phototheranostic performance characteristics of two structurally similar AIEgens (*i.e.*, TI and TSSI) were first explored using a multiscale modeling protocol that combines MD simulations and the PCM model. It is found that TSSI, which contains a thiophene-ring bridge to link the donor and acceptor moieties, shows largely improved phototheranostic properties that include a redshifted emission, a higher PCE and a good ISC efficiency. Therefore, TSSI has a better phototheranostic performance for PTI, PTT, PAI, and PDT compared with TI, which is consistent with experimental results.[36] Based on unraveling the structure–property relationship of TSSI, we propose a rational molecular design strategy, and further design a series of AIEgens *via* structural modification of the A moiety or by extending the π-bridge of TSSI. It is found that, relative to structural modification of the A moiety of TSSI, the lengthening of the π-bridge, particularly for TSSSSI, is predicted to provide a potential candidate for phototheranostic application owing to its excellent FLI, efficient ISC process, and emission spectrum in the NIR-II region. Lastly, the aggregation effects of the representative AIEgen TSSI were explored using a multiscale modelling protocol that combines MD simulations and the thermal vibration correlation function formalism coupled QM/MM model. It is demonstrated that the enhancement of the fluorescent quantum efficiency of representative TSSI was realized by blocking the excited-state non-radiative decay channels through suppressing the rotational vibrations in the low-frequency region. These calculations demonstrate a clear picture of the relationship between the molecular configuration, the molecular packing and the phototheranostic properties, which could provide valuable insight for the rational design of high-performance AIEgens for phototheranostics.

Conflicts of interest

The authors declare that they have no conflict of interest.

Acknowledgements

We thank the financially supporting of the Beijing Natural Science Foundation (Grant 2222027), the National Natural Science Foundation of China (Grants 22173006) and the Open Fund of Guangdong Provincial Key Laboratory of Luminescence from Molecular Aggregates (South China University of Technology, 2019B030301003), as well as the General Project of Chinese Academic Degrees and Graduate Education Society, grant number: 2020MSA431.

Notes and references

1 K. K. Ng and G. Zheng, Molecular Interactions in Organic Nanoparticles for Phototheranostic Applications, *Chem. Rev.*, 2015, **115**, 11012–11042.
2 S. Xu, Y. Duan and B. Liu, Precise Molecular Design for High-Performance Luminogens with Aggregation-Induced Emission, *Adv. Mater.*, 2020, **32**, 1903530.
3 J. Qi, H. Ou, Q. Liu and D. Ding, Gathering Brings Strength: How Organic Aggregates Boost Disease Phototheranostics, *Aggregate*, 2021, **2**, 95–113.
4 H. P. Wang, X. Chen, Y. L. Qi, L. W. Huang, C. X. Wang, D. Ding and X. Xue, Aggregation-Induced Emission (AIE)-Guided Dynamic Assembly for Disease Imaging and Therapy, *Adv. Drug Delivery Rev.*, 2021, **179**, 114028.
5 W. Xu, D. Wang and B. Tang, NIR-II AIEgens: A Win-Win Integration towards Bioapplications, *Angew. Chem., Int. Ed.*, 2021, **60**, 7476–7487.
6 A. Kalbasi, C. Komar, G. M. Tooker, M. Liu, J. W. Lee, W. L. Gladney, E. Ben-Josef and G. L. Beatty, Tumor-Derived

CCl_2 Mediates Resistance to Radiotherapy in Pancreatic Ductal Adenocarcinoma, *Clin. Cancer Res.*, 2017, **23**, 137–148.
7 D. De Ruysscher, G. Niedermann, N. G. Burnet, S. Siva, A. W. M. Lee and F. Hegi-Johnson, Radiotherapy Toxicity, *Nat. Rev. Dis. Primers*, 2019, **5**, 13.
8 B. R. Smith and S. S. Gambhir, Nanomaterials for in Vivo Imaging, *Chem. Rev.*, 2017, **117**, 901–986.
9 M. Gao, F. Yu, C. Lv, J. Choo and L. Chen, Fluorescent Chemical Probes for Accurate Tumor Diagnosis and Targeting Therapy, *Chem. Soc. Rev.*, 2017, **46**, 2237–2271.
10 Q. Fu, R. Zhu, J. Song, H. Yang and X. Chen, Photoacoustic Imaging: Contrast Agents and Their Biomedical Applications, *Adv. Mater.*, 2019, **31**, 1805875.
11 J. Weber, P. C. Beard and S. E. Bohndiek, Contrast Agents for Molecular Photoacoustic Imaging, *Nat. Methods*, 2016, **13**, 639–650.
12 F. Ren, Z. Li, K. Li, X. Zheng, J. Shi, C. Zhang, H. Guo, B. Tong, L. Xi, Z. Cai and Y. Dong, Donor Strategy for Promoting Nonradiative Decay to Achieve An Efficient Photothermal Therapy for Treating Cancer, *Sci. China: Chem.*, 2021, **64**, 1530–1539.
13 W. Shao, Q. Wei, S. Wang, F. Li, J. Wu, J. Ren, F. Cao, H. Liao, J. Gao, M. Zhou and D. Ling, Molecular Engineering of D–A–D Conjugated Small Molecule Nanoparticles for High Performance NIR-II Photothermal Therapy, *Mater. Horiz.*, 2020, **7**, 1379–1386.
14 Y. Liu, P. Bhattarai, Z. Dai and X. Chen, Photothermal Therapy and Photoacoustic Imaging via Nanotheranostics in Fighting Cancer, *Chem. Soc. Rev.*, 2019, **48**, 2053–2108.
15 F. He, G. Yang, P. Yang, Y. Yu, R. Lv, C. Li, Y. Dai, S. Gai and J. Lin, A New Single 808 nm NIR Light-Induced Imaging-Guided Multifunctional Cancer Therapy Platform, *Adv. Funct. Mater.*, 2015, **25**, 3966–3976.
16 Z. Chen, X. Mu, Z. Han, S. Yang, C. Zhang, Z. Guo, Y. Bai and W. He, An Optical/Photoacoustic Dual-Modality Probe: Ratiometric in/ex Vivo Imaging for Stimulated H_2S Upregulation in Mice, *J. Am. Chem. Soc.*, 2019, **141**, 17973–17977.
17 A. L. Antaris, H. Chen, K. Cheng, Y. Sun, G. Hong, C. Qu, S. Diao, Z. Deng, X. Hu, B. Zhang, X. Zhang, O. K. Yaghi, Z. R. Alamparambil, X. Hong, Z. Cheng and H. Dai, A Small-Molecule Dye for NIR-II Imaging, *Nat. Mater.*, 2016, **15**, 235–242.
18 S. Zhu, R. Tian, A. L. Antaris, X. Chen and H. Dai, Near-Infrared-II Molecular Dyes for Cancer Imaging and Surgery, *Adv. Mater.*, 2019, **31**, 1900321.
19 Y. Cai, Z. Wei, C. Song, C. Tang, W. Han and X. Dong, Optical Nano-Agents in the Second Near-Infrared Window for Biomedical Applications, *Chem. Soc. Rev.*, 2019, **48**, 22–37.
20 H. Qian, M. E. Cousins, E. H. Horak, A. Wakefield, M. D. Liptak and I. Aprahamian, Suppression of Kasha's Rule as A Mechanism for Fluorescent Molecular Rotors and Aggregation-Induced Emission, *Nat. Chem.*, 2017, **9**, 83–87.
21 Z. Sheng, B. Guo, D. Hu, S. Xu, W. Wu, W. H. Liew, K. Yao, J. Jiang, C. Liu, H. Zheng and B. Liu, Bright Aggregation-Induced-Emission Dots for Targeted Synergetic NIR-II Fluorescence and NIR-I Photoacoustic Imaging of Orthotopic Brain Tumors, *Adv. Mater.*, 2018, **30**, 1800766.
22 K. Deng, C. Li, S. Huang, B. Xing, D. Jin, Q. Zeng, Z. Hou and J. Lin, Recent Progress in Near Infrared Light Triggered Photodynamic Therapy, *Small*, 2017, **13**, 1702299.
23 M. Li, T. Xiong, J. Du, R. Tian, M. Xiao, L. Guo, S. Long, J. Fan, W. Sun, K. Shao, X. Song, J. W. Foley and X. Peng, Superoxide Radical Photogenerator with Amplification Effect: Surmounting the Achilles' Heels of Photodynamic Oncotherapy, *J. Am. Chem. Soc.*, 2019, **141**, 2695–2702.
24 M. Lan, S. Zhao, W. Liu, C. S. Lee, W. Zhang and P. Wang, Photosensitizers for Photodynamic Therapy, *Adv. Healthcare Mater.*, 2019, **8**, 1900132.
25 R. Hu, N. L. Leung and B. Z. Tang, AIE Macromolecules: Syntheses, Structures and Functionalities, *Chem. Soc. Rev.*, 2014, **43**, 4494–4562.
26 J. Mei, N. L. C. Leung, R. T. K. Kwok, J. W. Y. Lam and B. Z. Tang, Aggregation-Induced Emission: Together We Shine, United We Soar!, *Chem. Rev.*, 2015, **115**, 11718–11940.
27 H. Gao, X. Duan, D. Jiao, Y. Zeng, X. Zheng, J. Zhang, H. Ou, J. Qi and D. Ding, Boosting Photoacoustic Effect via Intramolecular Motions Amplifying Thermal-to-Acoustic Conversion Efficiency for Adaptive Image-Guided Cancer Surgery, *Angew. Chem., Int. Ed.*, 2021, **60**, 2–11.
28 S. Liu, C. Chen, Y. Li, H. Zhang, J. Liu, R. Wang, S. T. H. Wong, J. W. Y. Lam, D. Ding and B. Z. Tang, Constitutional Isomerization Enables Bright NIR-II AIEgen for Brain-Inflammation Imaging, *Adv. Funct. Mater.*, 2019, **30**, 1908125.
29 X. Ni, X. Zhang, X. Duan, H. L. Zheng, X. S. Xue and D. Ding, Near-Infrared Afterglow Luminescent Aggregation-Induced Emission Dots with Ultrahigh Tumor-to-Liver Signal Ratio for Promoted Image-Guided Cancer Surgery, *Nano Lett.*, 2019, **19**, 318–330.
30 J. Luo, Z. Xie, J. W. Lam, L. Cheng, H. Chen, C. Qiu, H. S. Kwok, X. Zhan, Y. Liu, D. Zhu and B. Z. Tang, Aggregation-Induced Emission of 1-Methyl-1,2,3,4,5-Pentaphenylsilole, *Chem. Commun.*, 2001, 1740–1741.
31 X. Zheng, Q. Peng, L. Zhu, Y. Xie, X. Huang and Z. Shuai, Unraveling the Aggregation Effect on Amorphous Phase AIE Luminogens: A Computational Study, *Nanoscale*, 2016, **8**, 15173–15180.
32 Y. Zeng, J. Yang and X. Zheng, Aggregation Effects on Photophysical Properties of NBN-Doped Polycyclic Aromatic Hydrocarbons: A Theoretical Study, *Phys. Chem. Chem. Phys.*, 2021, **23**, 23986–23997.
33 Y. Zeng, Y. Niu, Q. Peng and X. Zheng, Origin of Nonmonotonical Variation of Luminescence Efficiency under Pressure in Organic Molecule, *J. Phys. Chem. A*, 2022, **126**, 4147–4155.
34 J. Yang, Q. Peng, R. Xue, Z. Li and X. Zheng, Host–Guest Interaction-Induced Emission Enhancement of Amphiphilic AIEgens: A Computational Study, *Mater. Chem. Front.*, 2021, **5**, 1806–1816.
35 H. Wei, Y. Zeng, Q. Li and X. Zheng, Suppression of Reversible Photocyclization Reaction Induced Fluorescence

Enhancement: A Theoretical Study, *Phys. Chem. Chem. Phys.*, 2022, **24**, 25487–25494.

36 Z. Zhang, W. Xu, M. Kang, H. Wen, H. Guo, P. Zhang, L. Xi, K. Li, L. Wang, D. Wang and B. Z. Tang, An All-Round Athlete on the Track of Phototheranostics: Subtly Regulating the Balance between Radiative and Nonradiative Decays for Multimodal Imaging-Guided Synergistic Therapy, *Adv. Mater.*, 2020, **32**, 2003210.

37 J. Tomasi, B. Mennucci and R. Cammi, Quantum Mechanical Continuum Solvation Models, *Chem. Rev.*, 2005, **105**, 2999–3093.

38 S. Chibani, A. Charaf-Eddin, B. Le Guennic and D. Jacquemin, Boranil and Related NBO Dyes: Insights From Theory, *J. Chem. Theory Comput.*, 2013, **9**, 3127–3135.

39 Z. Shuai, Thermal Vibration Correlation Function Formalism for Molecular Excited State Decay Rates, *Chin. J. Chem.*, 2020, **38**, 1223–1232.

40 Z. Shuai and Q. Peng, Excited States Structure and Processes: Understanding Organic Light-Emitting Diodes at the Molecular Level, *Phys. Rep.*, 2014, **537**, 123–156.

41 Y. Niu, W. Li, Q. Peng, H. Geng, Y. Yi, L. Wang, G. Nan, D. Wang and Z. Shuai, Molecular Materials Property Prediction Package (MOMAP) 1.0: A Software Package for Predicting the Luminescent Properties and Mobility of Organic Functional Materials, *Mol. Phys.*, 2018, **116**, 1078–1090.

42 T. Zhang, Y. Jiang, Y. Niu, D. Wang, Q. Peng and Z. Shuai, Aggregation Effects on the Optical Emission of 1,1,2,3,4,5-Hexaphenylsilole (HPS): A QM/MM Study, *J. Phys. Chem. A*, 2014, **118**, 9094–9104.

43 T. Zhang, Q. Peng, C. Quan, H. Nie, Y. Niu, Y. Xie, Z. Zhao, B. Z. Tang and Z. Shuai, Using the Isotope Effect to Probe An Aggregation Induced Emission Mechanism: Theoretical Prediction and Experimental Validation, *Chem. Sci.*, 2016, **7**, 5573–5580.

44 Q. Wu, C. Deng, Q. Peng, Y. Niu and Z. Shuai, Quantum Chemical Insights into the Aggregation Induced Emission Phenomena: A QM/MM Study for Pyrazine Derivatives, *J. Comput. Chem.*, 2012, **33**, 1862–1869.

45 T. Zhang, H. Ma, Y. Niu, W. Li, D. Wang, Q. Peng, Z. Shuai and W. Liang, Spectroscopic Signature of the Aggregation-Induced Emission Phenomena Caused by Restricted Nonradiative Decay: A Theoretical Proposal, *J. Phys. Chem. C*, 2015, **119**, 5040–5047.